ACS OMEGA

http://pubs.acs.org/journal/acsodf

Article

Low Thermal Conductivity and Magneto-suppressed Thermal Transport in a Highly Oriented $FeSb_2$ Single Crystal

Zhong Chen, Xin Ding, and Mingxiang Xu*

Cite This: *ACS Omega* 2021, 6, 22681−22687

Read Online

ABSTRACT: Thermoelectric materials have been widely explored for the potential applications in power generation and refrigeration fields. High thermal conductivity (∼500 W/m K) of single-crystal $FeSb_2$ limits the application in cryogenic cooling. In this work, the $FeSb_2$ single crystal has been synthesized by the self-flux method. The rocking curve results reveal that the single crystal possesses quite high crystallinity. The micromorphology image shows that the single crystal is pyknotic without observable pores or cracks. Surprisingly, the thermal conductivity is reduced by 2 orders of magnitude compared with the previous reports, which can be attributed to the enhanced phonon scattering by the defects and impurities. Furthermore, the magnetic field can further suppress the thermal transport by reducing the phonon mean-free path. The maximum suppression rate of the thermal conductivity reaches 14% at 60 K when the magnetic field varies from 0 to 9 T. In this work, we have prepared the $FeSb_2$ single crystal with low thermal conductivity, and the magneto-suppressed thermal transport strategy can be applied to other thermoelectric materials.

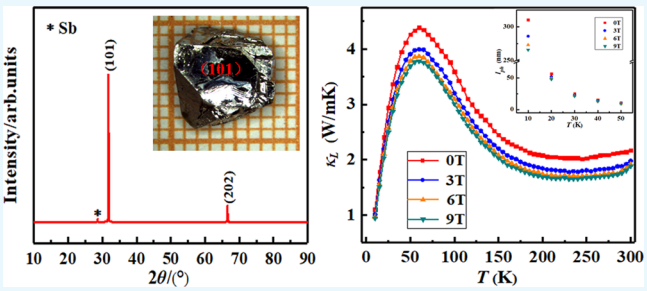

INTRODUCTION

The thermoelectric material, which can realize the interconversion between waste heat and electricity directly, has attracted widespread attention due to the promising applications for power generators and cryogenic cooling devices.[1−6] The thermoelectric efficiency mainly depends on the dimensionless thermoelectric figure of merit: $ZT = S^2\sigma T/\kappa$, where S, σ, and T refer to the Seebeck coefficient, electrical conductivity, and the absolute temperature, respectively.[7,8] $S^2\sigma$ is defined as the power factor.[9] κ is the thermal conductivity, which mainly includes the lattice thermal conductivity κ_L and the carrier thermal conductivity κ_c.[10,11] The high-performance thermoelectric materials should possess a high power factor and low thermal conductivity at a specific temperature.[12] Unfortunately, the coupling between these thermoelectric parameters (S, σ, and κ_c) makes it challenging to obtain high-performance thermoelectric materials.[13] Usually, there are two major strategies to improve the ZT value.[14] One method is to optimize the power factor through modulating carrier concentration with chemical doping,[15] band engineering,[16] resonant levels,[17] and energy barrier filtering.[18] The other approach emphasizes the reduction in thermal conductivity through alloying,[19] all-scale hierarchical architectures,[20] especially for nanostructuring.[21−23] Recently, magnetic interactions and spin fluctuation effects have been considered for improving thermoelectric properties.[24−28]

Strongly related $FeSb_2$, as a narrow gap semiconductor, possesses many fantastic phenomena at the low temperature.[29] $FeSb_2$ single crystals prepared by the self-flux method have been reported with supernormal physical properties. Petrovic et al.[30] found the anisotropy and large magnetoresistance effect in the $FeSb_2$ single crystal. Hu et al.[31] reported that the $FeSb_2$ single crystal possesses a giant mobility of ∼10^5 cm^2/V s at 8 K. Bentien et al.[32] observed a colossal Seebeck coefficient ∼−45,000 μV/K at 10 K and a power factor with the record high value of ∼2300 μW/cm K^2 at 12 K. Although single-crystal $FeSb_2$ possesses the ultrahigh Seebeck coefficient and excellent power factor in the cryogenic range, the ZT value is still quite low because of the unexpectedly high thermal conductivity.[33,34] Recently, meritorious research studies have been devoted to reduce the thermal conductivity, but mainly focused on the polycrystalline $FeSb_2$. For instance, Cu nanoparticles of ∼5 nm as a modulation dopant were introduced in the nanostructured $FeSb_2$, resulting in a reduction of thermal conductivity by Cu/$FeSb_2$ interfaces.[35] Zhao et al. found that reducing the grain size can significantly suppress the thermal conductivity, and an ultralow thermal conductivity of 0.34 W/m K was achieved at 50 K.[36] These studies mentioned above mainly introduced nanocomposites into polycrystalline $FeSb_2$ to reduce thermal conductivity.

Received: May 28, 2021
Accepted: August 16, 2021
Published: August 24, 2021

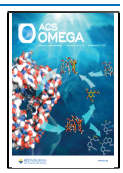

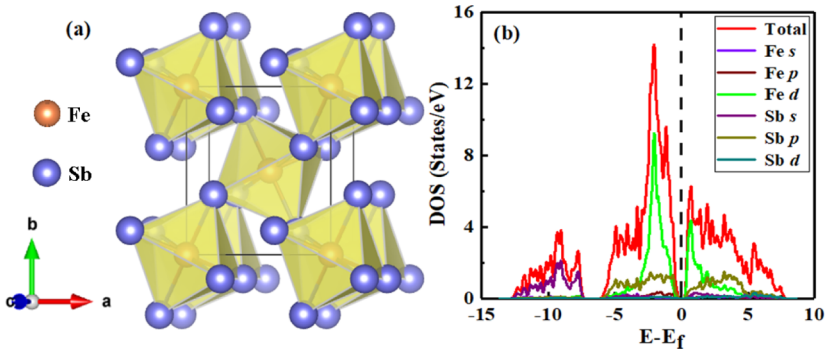

Figure 1. (a) Crystal structure of $FeSb_2$, and the octahedron is formed by the Fe atoms and the six Sb atoms. (b) Density of states of $FeSb_2$, and the Fermi level is indicated by a dashed line.

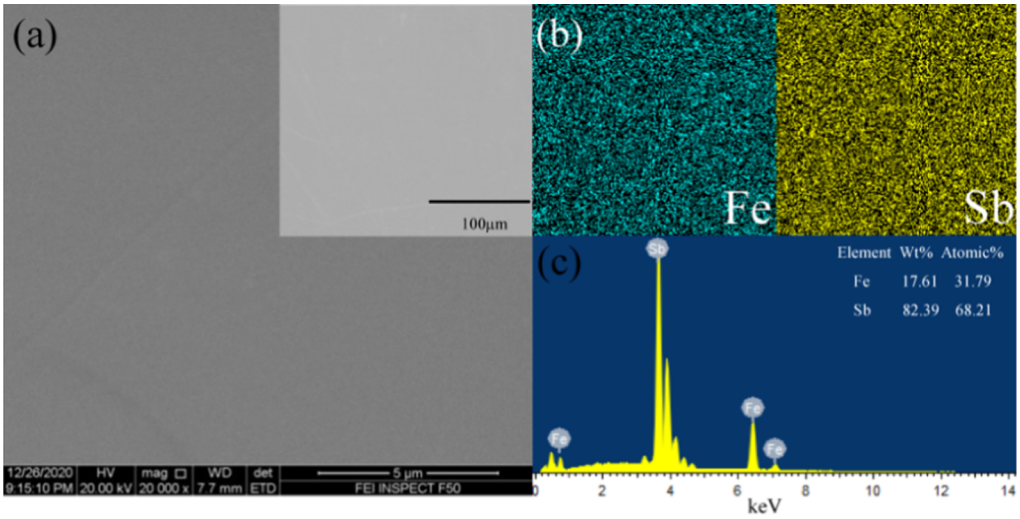

Figure 2. (a) SEM image, and the inset shows the selected area for element scanning. (b) Mapping images of Fe and Sb elements. (c) EDX spectrum with weight and atomic percentage.

However, the research on reducing the thermal conductivity of the $FeSb_2$ single crystal is rarely reported, especially for magneto-suppressed thermal conductivity. In this work, high-quality $FeSb_2$ single crystals were prepared by the self-flux method. The initial composition and the purity of starting materials are different from the previous reports,[32,34] which can result in the discrepant thermoelectric properties due to the defects and impurity effects.[37] Additionally, magneto-thermoelectric properties were investigated systematically, and we found that the magnetic field can further suppress the thermal conductivity in the case of impairing electrical transport performance slightly. This work provides a magneto-suppressed thermal conductivity strategy for other thermoelectric materials.

■ RESULTS AND DISCUSSION

Crystal and Electronic Structures. Figure 1a shows the crystal structure of $FeSb_2$ with the space group *Pnnm*.[38] The $FeSb_6$ octahedra share corners obliquely extending along the *ab*-plane, and Fe−Sb bond distances are equal in-plane. The other four Fe−Sb bond distances are distinct from the bond in the *ab*-plane. Moreover, the $FeSb_6$ aligns edge-sharing octahedra linearly along the orthorhombic *c*-axis.[39] Figure 1b presents the density of states of $FeSb_2$. The calculation results show that the Fe 3d-state and Sb-5p state play a major role on either side of the Fermi level, especially for the Fe 3d-state reaching a maximum. In the energy range from −12 to −6 eV, the Sb-5s state is predominant in the total density of states. The narrow energy gap is localized directly on the Fermi level, which indicates that $FeSb_2$ is the 3d-state semiconductor.[40]

Crystal Characterization and Orientation. Figure 2a shows the scanning electron microscopy (SEM) image of the single-crystal $FeSb_2$, which is magnified 20k times under high vacuum. It is obvious that the single crystal has fewer pores or cracks on the surface, indicating that the sample synthesized by the self-flux method is relatively condensed. The inset is the selected area for energy-dispersive X-ray spectroscopy (EDX) measurement. Subsequently, the corresponding elemental mapping images are shown in Figure 2b, which indicates that Fe and Sb elements distribute in the $FeSb_2$ homogeneously. Figure 2c presents the EDX spectrum of the square area (inset in Figure 2a), and it is clear that only Fe and Sb elements are detected and the atomic ratio is slightly off the nominal stoichiometric ratio of $FeSb_2$, which can be ascribed to the fact that the intrinsic point defects have been formed under the Sb-rich condition. In order to crossly validate the existence of point defects, the electron probe microanalysis (EPMA) was performed and the average value of 10 points was adopted. The average values of the atomic ratio for Fe and Sb are 32.84 and 67.16%, respectively, which can further confirm the formation of point defects.

https://doi.org/10.1021/acsomega.1c02803
ACS Omega 2021, 6, 22681−22687

The X-ray diffraction (XRD) pattern of the $FeSb_2$ single crystal is well detected, as shown in Figure 3a. The magnitude of the (101) peak intensity reaches 10^5, indicating that the single crystal possesses high crystallinity and is preferentially oriented along the (101) plane. The similar orientation character has been reported by Sun et al.[41] The low-intensity Sb peak is observed and marked by an asterisk, which can be ascribed to the existence of a small amount of Sb precipitates in the sample.[42] Figure 3b shows the morphology image of the $FeSb_2$ single crystal. It is clear that the single crystal has a large size and exhibits the metallic luster. To determine the orientation of the single crystal, the sample was detected by the high-resolution XRD (HRXRD). Figure 3c shows the rocking curve of the single crystal (200) peak, and the magnitude of the peak intensity reaches 10^4 with a full-width at half-maximum (fwhm) of 0.046°. Figure 3d exhibits the (040) diffraction peak near 56.1°, in which the peak intensity is 1 magnitude higher than that of the (200) peak. The fwhm of the (040) peak is 0.023°, which is only half of the (200) peak. Figure 3e shows the rocking curve of the (003) peak, in which the fwhm is 0.038°. The narrow fwhm of rocking curves illustrates that the single crystal possesses quite high crystallinity. Additionally, the crystal orientation and the lattice parameters can be determined according to the diffraction data. Figure 3f exhibits the abstract image of the single crystal.

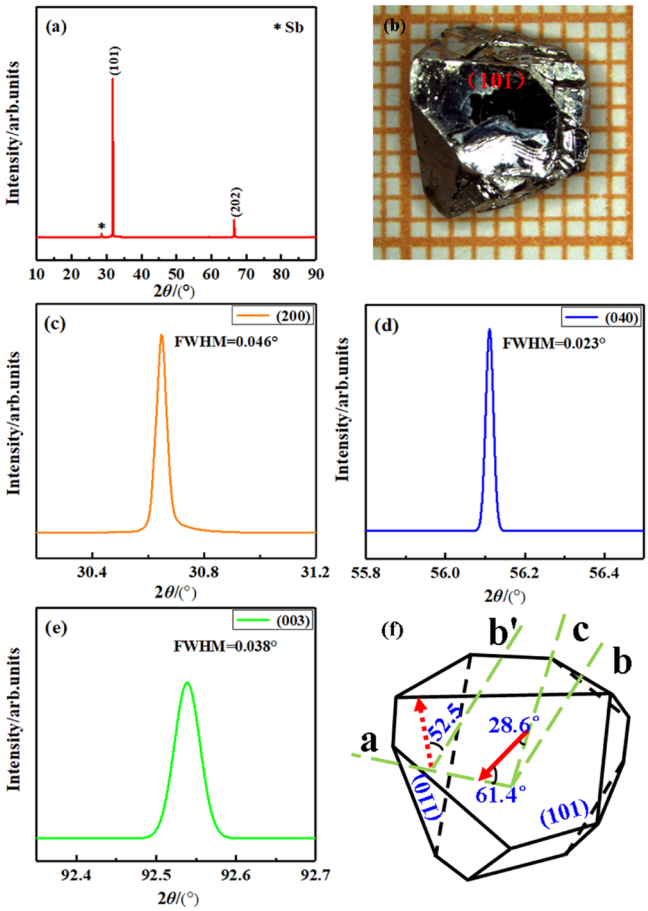

Figure 3. (a) XRD pattern of single-crystal $FeSb_2$. (b) Morphology image of single-crystal $FeSb_2$ prepared by the self-flux method. (c−e) Rocking curves of single-crystal $FeSb_2$ with (200), (040), and (003) peaks. (f) Abstract image with the definite directions.

It can be seen that the angle between the a-axis and the top of the solid arrow on the (101) plane is 61.4°. Simultaneously, an angle of 28.6° is observed between the end of the solid arrow and the c-axis. On the other detected (110) plane, the angle between the b'-axis and the end of the dashed arrow is 52.5°. Then, the complete rectangular coordinate system can be established after shifting the b'-axis to the b-axis position. The lattice parameters can be calculated according to the HRXRD data as follows: a = 5.8296 Å, b = 6.5512 Å, c = 3.1980 Å, and $\alpha = \beta = \gamma = 90°$, which is in reasonable agreement with the result reported earlier.[43]

Thermoelectric Properties. Considering the anisotropy of the $FeSb_2$ single crystal, the (101) plane was used for thermoelectric property measurement, and the magnetic field was perpendicular to the (101) plane throughout the measurement process (Supporting Information, Figure S1). Figure 4a exhibits the temperature dependence of the Seebeck coefficient. The absolute values of the Seebeck coefficient increase first and then decrease with the increased temperature. Additionally, the Seebeck coefficient values decrease slightly with the increase in magnetic field. The maximum Seebeck coefficient reaches −183 μV/K at 30 K with a magnetic field of 0 T, which is much lower than that of the previous report.[32,44] The comparisons of the Seebeck coefficient can be observed in Supporting Information, Figure S2a. The obvious diversity can be ascribed to the fact that the intrinsic point defects in the sample enhance the phonon scattering and weaken the phonon-drag effect significantly.[45,46] Additionally, owing to the fact that the purity of starting materials is lower than that of previous reports,[32,34] the influence of impurity effects can be another reason for the reduction of the Seebeck coefficient.[37] The approximation of $T_{max} \approx \theta_D/10$ is consistent with the Seebeck coefficient measurement.[46] The T_{max} is the temperature (30 K) at which the Seebeck peak occurs, and the θ_D refers to the Debye temperature (327 K, provided in the thermal conductivity discussion). The inset shows the variation of the Seebeck coefficient measured from 10 to 300 K. The sign of the Seebeck coefficient changes at around 150 K, indicating that the major carrier changes from electrons to holes. A similar phenomenon has been reported by Kieslich et al.[47] A room temperature Seebeck coefficient ∼20 μV/K is obtained at different magnetic fields, which is slightly lower than the reported value (∼26 μV/K).[46]

Figure 4b shows the electrical conductivity versus temperature curves at different magnetic fields. The electrical conductivity is relatively low at the low temperature, which can be attributed to the low carrier concentration (Supporting Information, Figure S3). The electrical conductivity increases constantly with the increased temperature, which indicates that the $FeSb_2$ single crystal exhibits the semiconductor behavior.[29] The resistivity ρ (inverse of the electrical conductivity) is higher than that of the previous reports (Figure S2b in Supporting Information),[32,34,37] which may be ascribed to the enhancement of the carrier scattering by the defects and impurities, and then results in the decrease in carrier mobility. The electrical conductivity decreases slightly as the magnetic field increases, which demonstrates that the sample possesses a positive magnetoresistance effect.[48] Besides, the identical trend of electrical conductivity indicates that the conductive mechanism is almost unchanged after introducing the magnetic field. To further understand the conductive mechanism, the resistivity data have been fitted by two models in different temperature regions, as shown in the inset of Figure 4b. In the

https://doi.org/10.1021/acsomega.1c02803
ACS Omega 2021, 6, 22681−22687

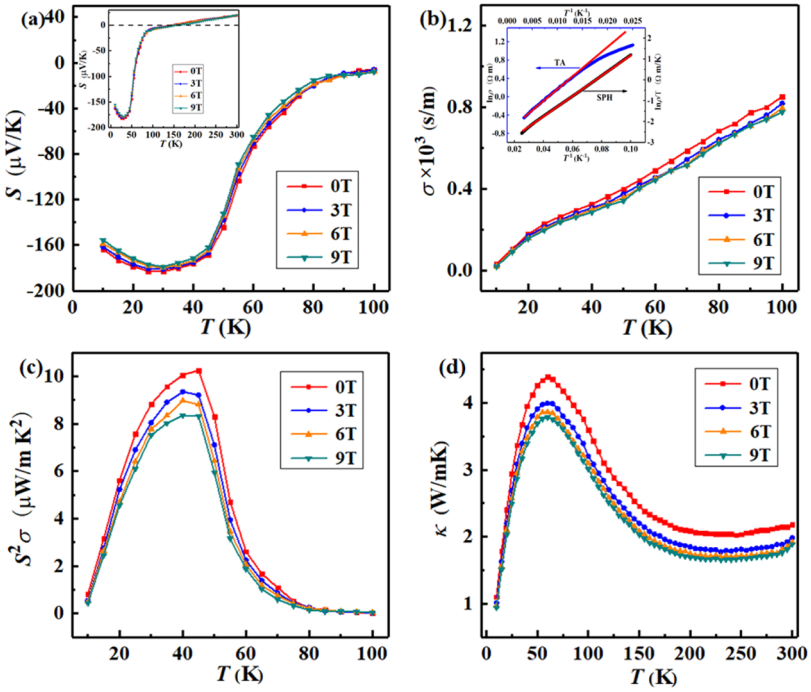

Figure 4. Temperature-dependent thermoelectric properties of single-crystal $FeSb_2$: (a) Seebeck coefficient S; (b) electrical conductivity σ; the inset shows the fitting results of $\ln \rho - T^{-1}$ and $\ln \rho/T - T^{-1}$ at 0 T; (c) power factor $S^2\sigma$; and (d) thermal conductivity κ.

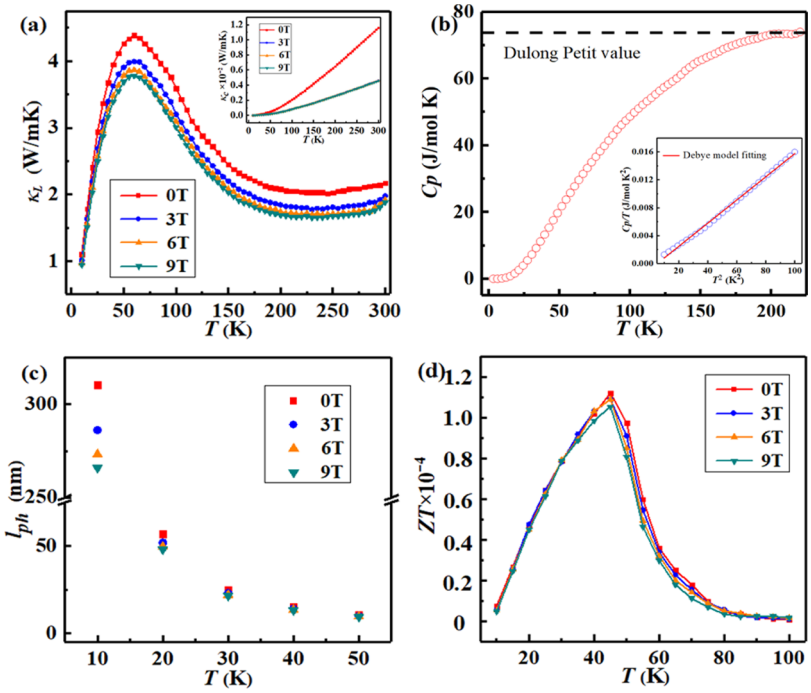

Figure 5. (a) Temperature-dependent lattice thermal conductivity κ_L, the inset shows the carrier thermal conductivity κ_c. (b) Specific heat per mole $FeSb_2$ as a function of temperature, the inset shows the Debye model fitting in the low-temperature range. (c) Phonon mean-free path vs temperature below 50 K. (d) Variation of ZT vs the temperature.

temperature range from 10 to 40 K, the conductive mechanism is well fitted with the adiabatic small polaron hopping (SPH) model, which can be explained by the expression: $\rho = \rho_0 T \exp(E_A/k_B T)$.[49] When the temperature is above 40 K, the conductive mechanism is more consistent with the thermal activation (TA) model, which can be expressed by the formula: $\rho = \rho_0 \exp(E_A/k_B T)$,[50] where E_A refers to the energy difference between the intermediate and initial states, and the E_A values of SPH and TA models are 4.23 and 8.28 meV, respectively. k_B is the Boltzmann constant, and ρ_0 is the pre-exponential factor. Figure 4c exhibits the power factor as a function of the temperature. It is obvious that the power factor increases first and then decreases with the increase in temperature. A maximum power factor (10.26 μW/m K^2) is obtained at 45 K with a magnetic field of 0 T, which is lower than the record high value reported by Bentien et al.[32] (shown in Supporting

https://doi.org/10.1021/acsomega.1c02803
ACS Omega 2021, 6, 22681−22687

Information, Figure S2c). The relationship between the thermal conductivity and the temperature is depicted in Figure 4d. The maximum thermal conductivity is only 4.39 W/m K at 60 K with a magnetic field of 0 T, which is 2 orders of magnitude smaller than that of the single crystal reported in previous research studies (Supporting Information, Figure S2d).[32,34] The low thermal conductivity is originated from the enhanced phonon scattering by the defects and impurities. Furthermore, it is noteworthy that the thermal conductivity can be further suppressed with the increase in the magnetic field, and the maximum suppression rate of the thermal conductivity is 14% at 60 K when the magnetic field varies from 0 to 9 T.

To explore the effect of the magnetic field on thermal conductivity, the κ_c and κ_L were investigated in detail. According to the Wiedemann−Franz law, the κ_c can be calculated using the equation: $\kappa_c = L\sigma T$, where L is the Lorentz number (2.44×10^{-8} WΩ K^{-2}).[32] As shown in the inset of Figure 5a, the κ_c decreases as the magnetic field increases. Due to the fact that the magnitude order of the κ_c is quite low, it illustrates that the κ is mainly contributed by the κ_L.[47] Subsequently, the κ_L can be obtained from κ by subtracting the κ_c, as shown in Figure 5a. To further explore the effect of the magnetic field on the κ_L, the heat capacity was measured at 0 and 9 T. Figure 5b only shows the heat capacity at 0 T due to the fact that heat capacity hardly changes under different magnetic fields in the entire temperature range. The classical Dulong Petit value $3NR$ = 74.8 J/mol K is marked by the dotted line, where N is the number of atoms per formula unit and R refers to the gas constant.[51] The inset depicts the fitting curves in low-temperature data using the Debye model, which can be expressed by $C_p/T = \gamma + \beta T^2$, where γ is the electronic specific heat coefficient and β is a constant containing a factor of the θ_D. According to the fitting results, the θ_D can be calculated using the formula: $\theta_D = (12\pi^4 NR/5\beta)^{1/3}$.[52] In the $FeSb_2$ sample prepared by the self-flux method, the θ_D is calculated at 327 K, which is lower than the value of previous research.[51] Then, a sound velocity ν of 2973 m/s is evaluated from $\theta_D/\nu = h/k_B[(3dNN_A)/(4\pi M)]^{1/3}$, where h is the Planck constant, N_A is Avogadro's number, d is the density, and M is the molar mass. According to the phonon velocity and the constant-volume specific heat C_V, the phonon mean-free path l_{ph} can be calculated using $l_{ph} = 3\kappa_L/\nu C_V$.[53] Figure 5c shows the variation of the l_{ph} in different magnetic fields at 10−50 K. The maximum l_{ph} (310 nm) is obtained at 10 K with a magnetic field of 0 T, which is much smaller than that of the previous report.[54] It can be attributed to the fact that the defects and impurities in the sample enhance the scattering of phonons, then reducing the l_{ph} significantly. Moreover, the l_{ph} can be further suppressed by the magnetic field. Especially, the suppression is more obvious in the low-temperature region. The maximum suppression rate of the phonon mean-free path achieves 14.4% at 10 K when the magnetic field varies from 0 to 9 T. Figure 5d shows the variation of ZT values with different magnetic fields below 100 K. Although the κ is reduced significantly and further suppressed by the magnetic field, the ZT value is not enhanced due to the decrease in the Seebeck coefficient and electrical conductivity with the increased magnetic field.

■ CONCLUSIONS

In this work, a high-quality $FeSb_2$ single crystal was synthesized by the self-flux method. The crystal characterization and magneto-thermoelectric properties have been investigated systematically. The XRD results indicate that the $FeSb_2$ single crystal is highly oriented along the (101) plane. The rocking curves suggest that the single crystal possesses high crystallinity, and the SEM analysis demonstrates that the sample is relatively condensed. The thermal conductivity decreases significantly due to the enhanced phonon scattering by the defects and impurities. Moreover, the thermal conductivity can be further suppressed by 14% at 60 K when the magnetic field varies from 0 to 9 T. Although the thermal conductivity is reduced significantly and further suppressed by the magnetic field, the ZT value is not enhanced due to the slight decrease in the Seebeck coefficient and electrical conductivity with the increased magnetic field. Future efforts will be desired to improve the ZT value of the $FeSb_2$ single crystal through enhancing the power factor to realize the cryogenic cooling application.

■ EXPERIMENTAL SECTION

Preparation and Characterization. The $FeSb_2$ single crystal was fabricated by mixing Fe (chunks, 99.98%) and Sb (grains, 99.99%) according to the stoichiometric ratio $Fe_{0.09}Sb_{0.91}$ in a vacuum quartz ampule. The sealed ampule was heated to 1373 K with a rate of 3.6 K/min and held at the temperature for 10 h. Then, the quartz ampule was cooled to 923 K in 3 h, subsequently increased to 1033 K in 1 h. After that, the furnace was slowly cooled to 933 K in 100 h. Finally, the $FeSb_2$ single crystal was separated from the Sb flux by centrifugation. The crystal phase was checked using the XRD (Rigaku SmartLab) with Cu Kα radiation. Moreover, the HRXRD (Bruker D8 Discover) was utilized for crystalline orientation. The surface topography was observed by SEM (FEI Inspect F50), which was equipped with the EDX (Oxford Inca X-act). Furthermore, the EPMA (JXA-8230) was executed to quantify the accurate content of each element in the sample. The thermoelectric properties were measured in the thermal transport option by the physical property measurement system (PPMS-9, Quantum Design).

Computational Details. To understand the electronic structure of the $FeSb_2$ crystal, the first-principle calculations based on the density functional theory were performed by the Vienna Ab initio Simulation Package (VASP).[55] The local density approximation plus U was employed to calculate the electronic structure due to the Hartree-type Coulomb interaction.[56] The interaction between the core ion and valence electrons was described by the projector augmented wave method.[57] A plane-wave cutoff energy of 500 eV was set, and a 5 × 5 × 10 k-point mesh was adopted for sampling the Brillouin zone. A convergence energy of 10^{-6} eV was used, and the maximal force of each atom was relaxed to less than 0.01 eV/Å.

■ ASSOCIATED CONTENT

Supporting Information

The Supporting Information is available free of charge at https://pubs.acs.org/doi/10.1021/acsomega.1c02803.

Experimental setup, comparative analysis, and carrier concentrations (PDF)

https://doi.org/10.1021/acsomega.1c02803
ACS Omega 2021, 6, 22681−22687

AUTHOR INFORMATION

Corresponding Author

Mingxiang Xu − *School of Physics, Southeast University, Nanjing 211189, China*; orcid.org/0000-0002-6869-8500; Email: mxxu@seu.edu.cn

Authors

Zhong Chen − *School of Physics, Southeast University, Nanjing 211189, China*

Xin Ding − *School of Physics, Southeast University, Nanjing 211189, China*

Complete contact information is available at: https://pubs.acs.org/10.1021/acsomega.1c02803

Notes

The authors declare no competing financial interest.

ACKNOWLEDGMENTS

This work is financially supported by the Natural Science Foundation of Jiangsu Province of China (grant no. BK20201285). The authors are grateful to the computational resources from the Big Data Center of Southeast University. We are also grateful to Shanghai Institute of Ceramics, Chinese Academy of Sciences for assistance with the high-resolution XRD measurement.

REFERENCES

(1) Bell, L. E. Cooling, heating, generating power, and recovering waste heat with thermoelectric systems. *Science* **2008**, *321*, 1457−1461.

(2) Snyder, G. J.; Toberer, E. S. Complex thermoelectric materials. *Nat. Mater.* **2008**, *7*, 105−114.

(3) Su, X.; Wei, P.; Li, H.; Liu, W.; Yan, Y.; Li, P.; Su, C.; Xie, C.; Zhao, W.; Zhai, P.; Zhang, Q.; Tang, X.; Uher, C. Multi-scale microstructural thermoelectric materials: transport behavior, non-equilibrium preparation, and applications. *Adv. Mater.* **2017**, *29*, 1602013.

(4) Hu, Y.; Yang, T.; Li, D.; Ding, G.; Dun, C.; Wu, D.; Wang, X. Origins of minimized lattice thermal conductivity and enhanced thermoelectric performance in WS_2/WSe_2 lateral superlattice. *ACS Omega* **2021**, *6*, 7879.

(5) Petsagkourakis, I.; Tybrandt, K.; Crispin, X.; Ohkubo, I.; Satoh, N.; Mori, T. Thermoelectric materials and applications for energy harvesting power generation. *Sci. Technol. Adv. Mater.* **2018**, *19*, 836−862.

(6) Mao, J.; Zhu, H.; Ding, Z.; Liu, Z.; Gamage, G. A.; Chen, G.; Ren, Z. High thermoelectric cooling performance of n-type Mg_3Bi_2-based materials. *Science* **2019**, *365*, 495−498.

(7) Ahmed, A. J.; Hossain, M. S. A.; Kazi Nazrul Islam, S. M.; Yun, F.; Yang, G.; Hossain, R.; Khan, A.; Na, J.; Eguchi, M.; Yamauchi, Y.; Wang, X. Significant improvement in electrical conductivity and figure of merit of nanoarchitectured porous $SrTiO_3$ by La doping optimization. *ACS Appl. Mater. Interfaces* **2020**, *12*, 28057−28064.

(8) Hyun, C.-M.; Choi, J.-H.; Lee, S.-W.; Seo, S.-Y.; Lee, M.-J.; Kwon, S.-H.; Ahn, J.-H. Synthesis of Bi_2Te_3 single crystals with lateral size up to tens of micrometers by vapor transport and its potential for thermoelectric applications. *Cryst. Growth Des.* **2019**, *19*, 2024.

(9) Guo, Q.; Son, H.-W.; Mori, T. Rational design of spinel-type $Cu_4Mn_2Te_4$/TMTe (TM = Co, Ni) composites with synergistically manipulated electrical and thermal transport properties. *ACS Appl. Energy Mater.* **2020**, *3*, 2096−2102.

(10) Xing, Y.; Liu, R.; Liao, J.; Zhang, Q.; Xia, X.; Wang, C.; Huang, H.; Chu, J.; Gu, M.; Zhu, T.; Zhu, C.; Xu, F.; Yao, D.; Zeng, Y.; Bai, S.; Uher, C.; Chen, L. High-efficiency half-Heusler thermoelectric modules enabled by self-propagating synthesis and topologic structure optimization. *Energy Environ. Sci.* **2019**, *12*, 3390−3399.

(11) Deng, S.; Liu, H.; Li, D.; Wang, J.; Cheng, F.; Shen, L.; Deng, S. Thermoelectric properties of Sr-filled Ge-based type I single-crystal clathrate grown by Sn-flux method. *J. Electron. Mater.* **2017**, *46*, 2662−2667.

(12) Xiao, Y.; Li, W.; Chang, C.; Chen, Y.; Huang, L.; He, J.; Zhao, L.-D. Synergistically optimizing thermoelectric transport properties of n-type PbTe via Se and Sn co-alloying. *J. Alloys Compd.* **2017**, *724*, 208−221.

(13) Zhu, T.; Liu, Y.; Fu, C.; Heremans, J. P.; Snyder, J. G.; Zhao, X. Compromise and synergy in high-efficiency thermoelectric materials. *Adv. Mater.* **2017**, *29*, 1605884.

(14) Chen, Z.-G.; Han, G.; Yang, L.; Cheng, L.; Zou, J. Nanostructured thermoelectric materials: Current research and future challenge. *Prog. Nat. Sci.* **2012**, *22*, 535−549.

(15) Luo, Y.; Zheng, Y.; Luo, Z.; Hao, S.; Du, C.; Liang, Q.; Li, Z.; Khor, K. A.; Hippalgaonkar, K.; Xu, J.; Yan, Q.; Wolverton, C.; Kanatzidis, M. G. n-type $SnSe_2$ oriented-nanoplate-based pellets for high thermoelectric performance. *Adv. Energy Mater.* **2018**, *8*, 1702167.

(16) Pei, Y.; Shi, X.; LaLonde, A.; Wang, H.; Chen, L.; Snyder, G. J. Convergence of electronic bands for high performance bulk thermoelectrics. *Nature* **2011**, *473*, 66−69.

(17) Chen, Z.; Tang, Y.; Li, D.; Liu, J.; Shen, L.; Liu, W.; Sun, L.; Deng, S. Enhancement of electrical performance via carrier modulation in single crystalline PbTe prepared by Pb-flux method. *J. Alloys Compd.* **2019**, *774*, 282−289.

(18) Martin, J.; Wang, L.; Chen, L.; Nolas, G. S. Enhanced Seebeck coefficient through energy-barrier scattering in PbTe nanocomposites. *Phys. Rev. B: Condens. Matter Mater. Phys.* **2009**, *79*, 115311.

(19) Tan, G.; Shi, F.; Hao, S.; Chi, H.; Bailey, T. P.; Zhao, L.-D.; Uher, C.; Wolverton, C.; Dravid, V. P.; Kanatzidis, M. G. Valence band modification and high thermoelectric performance in SnTe heavily alloyed with MnTe. *J. Am. Chem. Soc.* **2015**, *137*, 11507−11516.

(20) Biswas, K.; He, J.; Blum, I. D.; Wu, C.-I.; Hogan, T. P.; Seidman, D. N.; Dravid, V. P.; Kanatzidis, M. G. High-performance bulk thermoelectrics with all-scale hierarchical architectures. *Nature* **2012**, *489*, 414−418.

(21) Koumoto, K.; Mori, T. *Thermoelectric Nanomaterials*; Springer: Heidelberg, Germany, 2013; pp 177−191.

(22) Yang, G.; Sang, L.; Yun, F. F.; Mitchell, D. R. G.; Casillas, G.; Ye, N.; See, K.; Pei, J.; Wang, X.; Li, J. F.; Snyder, G. J.; Wang, X. Significant enhancement of thermoelectric figure of merit in BiSbTe-based composites by incorporating carbon microfiber. *Adv. Funct. Mater.* **2021**, *31*, 2008851.

(23) Yang, G.; Niu, R.; Sang, L.; Liao, X.; Mitchell, D. R. G.; Ye, N.; Pei, J.; Li, J. F.; Wang, X. Ultra-high thermoelectric performance in bulk BiSbTe/amorphous boron composites with nano-defect architectures. *Adv. Energy Mater.* **2020**, *10*, 2000757.

(24) Zhao, W.; Liu, Z.; Sun, Z.; Zhang, Q.; Wei, P.; Mu, X.; Zhou, H.; Li, C.; Ma, S.; He, D.; Ji, P.; Zhu, W.; Nie, X.; Su, X.; Tang, X.; Shen, B.; Dong, X.; Yang, J.; Liu, Y.; Shi, J. Superparamagnetic enhancement of thermoelectric performance. *Nature* **2017**, *549*, 247−251.

(25) Chang, H.; Gui, X.; Huang, S.; Nepal, R.; Chapai, R.; Xing, L.; Xie, W.; Jin, R. Mn-induced ferromagnetism and enhanced thermoelectric properties in $Ru_{1-x}Mn_xSb_{2+\delta}$. *New J. Phys.* **2019**, *21*, 033008.

(26) Zhao, L.; Chen, C.; Pan, L.; Hu, X.; Lu, C.; Wang, Y. Magnetic iron doping in Cu_2SnS_3 ceramics for enhanced thermoelectric transport properties. *J. Appl. Phys.* **2019**, *125*, 095107.

(27) Vaney, J.-B.; Aminorroaya Yamini, S.; Takaki, H.; Kobayashi, K.; Kobayashi, N.; Mori, T. Magnetism-mediated thermoelectric performance of the Cr-doped bismuth telluride tetradymite. *Mater. Today Phys.* **2019**, *9*, 100090.

(28) Tsujii, N.; Nishide, A.; Hayakawa, J.; Mori, T. Observation of enhanced thermopower due to spin fluctuation in weak itinerant ferromagnet. *Sci. Adv.* **2019**, *5*, No. eaat5935.

(29) Kassem, M. A.; Tabata, Y.; Waki, T.; Nakamura, H. Drastic effect of the Mn-substitution in the strongly correlated semiconductor $FeSb_2$. *J. Phys.: Conf. Ser.* **2017**, *868*, 012019.
(30) Petrovic, C.; Kim, J. W.; Bud'ko, S. L.; Goldman, A. I.; Canfield, P. C.; Choe, W.; Miller, G. J. Anisotropy and large magnetoresistance in the narrow-gap semiconductor $FeSb_2$. *Phys. Rev. B: Condens. Matter Mater. Phys.* **2003**, *67*, 155205.
(31) Hu, R.; Mitrović, V. F.; Petrovic, C. Giant carrier mobility in single crystals of $FeSb_2$. *Appl. Phys. Lett.* **2008**, *92*, 182108.
(32) Bentien, A.; Johnsen, S.; Madsen, G. K. H.; Iversen, B. B.; Steglich, F. Colossal Seebeck coefficient in strongly correlated semiconductor $FeSb_2$. *Europhys. Lett.* **2007**, *80*, 17008.
(33) Sun, P.; Oeschler, N.; Johnsen, S.; Iversen, B. B.; Steglich, F. Thermoelectric properties of the narrow-gap semiconductors $FeSb_2$ and $RuSb_2$: A comparative study. *J. Phys.: Conf. Ser.* **2009**, *150*, 012049.
(34) Wang, K.; Hu, R.; Warren, J.; Petrovic, C. Enhancement of the thermoelectric properties in doped $FeSb_2$ bulk crystals. *J. Appl. Phys.* **2012**, *112*, 013703.
(35) Koirala, M.; Zhao, H.; Pokharel, M.; Chen, S.; Dahal, T.; Opeil, C.; Chen, G.; Ren, Z. Thermoelectric property enhancement by Cu nanoparticles in nanostructured $FeSb_2$. *Appl. Phys. Lett.* **2013**, *102*, 213111.
(36) Zhao, H.; Pokharel, M.; Zhu, G.; Chen, S.; Lukas, K.; Jie, Q.; Opeil, C.; Chen, G.; Ren, Z. Dramatic thermal conductivity reduction by nanostructures for large increase in thermoelectric figure-of-merit of $FeSb_2$. *Appl. Phys. Lett.* **2011**, *99*, 163101.
(37) Takahashi, H.; Yasui, Y.; Terasaki, I.; Sato, M. Effects of ppm-level imperfection on the transport properties of $FeSb_2$ single crystals. *J. Phys. Soc. Jpn.* **2011**, *80*, 054708.
(38) Koyama, T.; Nakamura, H.; Kohara, T.; Takahashi, Y. Magnetization process of narrow-gap semiconductor $FeSb_2$. *J. Phys. Soc. Jpn.* **2010**, *79*, 093704.
(39) Tan, X.; Devlin, K. P.; Deng, X.; Kang, C.-J.; Croft, M.; Frank, C. E.; Pak, C.; Lapidus, S.; Kauzlarich, S. M.; Taufour, V.; Kotliar, G.; Greenblatt, M. Thermoelectric properties of CoAsSb: an experimental and theoretical study. *Chem. Mater.* **2018**, *30*, 4207−4215.
(40) Petrovic, C.; Lee, Y.; Vogt, T.; Lazarov, N. D.; Bud'ko, S. L.; Canfield, P. C. Kondo insulator description of spin state transition in $FeSb_2$. *Phys. Rev. B: Condens. Matter Mater. Phys.* **2005**, *72*, 045103.
(41) Sun, Y.; Johnsen, S.; Eklund, P.; Sillassen, M.; Bøttiger, J.; Oeschler, N.; Sun, P.; Steglich, F.; Iversen, B. B. Thermoelectric transport properties of highly oriented $FeSb_2$ thin films. *J. Appl. Phys.* **2009**, *106*, 033710.
(42) Sanchela, A. V.; Thakur, A. D.; Tomy, C. V. Enhancement in thermoelectric properties of $FeSb_2$ by Sb site deficiency. *J. Materiomics* **2015**, *1*, 205−212.
(43) Cao, Y.; Yuan, S.; Liu, M.; Kang, B.; Lu, B.; Zhang, J.; Cao, S. High quality $FeSb_2$ single crystal growth by the gradient freeze technique. *J. Cryst. Growth* **2013**, *363*, 128−131.
(44) Sun, P.; Oeschler, N.; Johnsen, S.; Iversen, B. B.; Steglich, F. Huge thermoelectric power factor: $FeSb_2$ versus $FeAs_2$ and $RuSb_2$. *Appl. Phys. Express* **2009**, *2*, 091102.
(45) Matsuura, H.; Maebashi, H.; Ogata, M.; Fukuyama, H. Effect of phonon drag on seebeck coefficient based on linear response theory: application to $FeSb_2$. *J. Phys. Soc. Jpn.* **2019**, *88*, 074601.
(46) Pokharel, M.; Zhao, H.; Lukas, K.; Ren, Z.; Opeil, C.; Mihaila, B. Phonon drag effect in nanocomposite $FeSb_2$. *MRS Commun.* **2013**, *3*, 31−36.
(47) Kieslich, G.; Birkel, C. S.; Veremchuk, I.; Grin, Y.; Tremel, W. Thermoelectric properties of spark-plasma sintered nanoparticular $FeSb_2$ prepared via a solution chemistry approach. *Dalton Trans.* **2014**, *43*, 558.
(48) Hu, R. W.; Thomas, K. J.; Lee, Y.; Vogt, T.; Choi, E. S.; Mitrovic, V. F.; Hermann, R. P.; Grandjean, F.; Canfield, P. C.; Kim, J. W.; Goldman, A. I.; Petrovic, C. Colossal positive magnetoresistance in a doped nearly magnetic semiconductor. *Phys. Rev. B: Condens. Matter Mater. Phys.* **2008**, *77*, 085212.
(49) Li, Q.; Xing, L.; Xu, M. Magnetic properties, resistivity and magnetoresistance effects of double perovskite $La_2Co_{1-x}Fe_xMnO_6$. *J. Alloys Compd.* **2017**, *710*, 771−777.
(50) Wei, K.; Martin, J.; Nolas, G. S. Synthesis, SPS processing and low temperature transport properties of polycrystalline $FeSb_2$ with nano-scale grains. *Mater. Lett.* **2014**, *122*, 289−291.
(51) Bentien, A.; Madsen, G. K. H.; Johnsen, S.; Iversen, B. B. Experimental and theoretical investigations of strongly correlated $FeSb_{2-x}Sn_x$. *Phys. Rev. B: Condens. Matter Mater. Phys.* **2006**, *74*, 205105.
(52) Tan, G.; Liu, W.; Chi, H.; Su, X.; Wang, S.; Yan, Y.; Tang, X.; Wong-Ng, W.; Uher, C. Realization of high thermoelectric performance in p-type unfilled ternary skutterudites $FeSb_{2+x}Te_{1-x}$ via band structure modification and significant point defect scattering. *Acta Mater.* **2013**, *61*, 7693−7704.
(53) Du, Q. H.; Guzman, D.; Choi, S.; Petrovic, C. Crystal size effects on giant thermopower in $CrSb_2$. *Phys. Rev. B* **2020**, *101*, 035125.
(54) Sun, P.; Oeschler, N.; Johnsen, S.; Iversen, B. B.; Steglich, F. $FeSb_2$: Prototype of huge electron-diffusion thermoelectricity. *Phys. Rev. B: Condens. Matter Mater. Phys.* **2009**, *79*, 153308.
(55) Kresse, G.; Furthmüller, J. Efficient iterative schemes for ab initio total-energy calculations using a plane-wave basis set. *Phys. Rev. B: Condens. Matter Mater. Phys.* **1996**, *54*, 11169.
(56) Park, J.; Xia, Y.; Ozoliņš, V. First-principles assessment of thermoelectric properties of $CuFeS_2$. *J. Appl. Phys.* **2019**, *125*, 125102.
(57) Torrent, M.; Jollet, F.; Bottin, F.; Zérah, G.; Gonze, X. Implementation of the projector augmented-wave method in the ABINIT code: application to the study of iron under pressure. *Comput. Mater. Sci.* **2008**, *42*, 337−351.

https://doi.org/10.1021/acsomega.1c02803
ACS Omega 2021, 6, 22681−22687